Elastic shear wave scattering by randomly rough surfaces

Stewart G Haslinger[a], Michael J S Lowe[a], Peter Huthwaite[a], Richard V Craster[b], Fan Shi[c,*]

[a]*Department of Mechanical Engineering, Imperial College, London*
[b]*Department of Mathematics, Imperial College, London*
[c]*Department of Mechanical and Aerospace Engineering, Hong Kong University of Science and Technology*

Abstract

Characterizing cracks within elastic media forms an important aspect of ultrasonic non-destructive evaluation (NDE) where techniques such as time-of-flight diffraction and pulse-echo are often used with the presumption of scattering from smooth, straight cracks. However, cracks are rarely straight, or smooth, and recent attention has focussed upon rough surface scattering primarily by longitudinal wave excitations.

We provide a comprehensive study of scattering by incident shear waves, thus far neglected in models of rough surface scattering despite their practical importance in the detection of surface-breaking defects, using modelling, simulation and supporting experiments. The scattering of incident shear waves introduces challenges, largely absent in the longitudinal case, related to surface wave mode-conversion, the reduced range of validity of the Kirchhoff approximation (KA) as compared with longitudinal incidence, and an increased importance of correlation length.

The expected reflection from a rough defect is predicted using a statistical model from which, given the angle of incidence and two statistical parameters, the expected reflection amplitude is obtained instantaneously for any scattering angle and length of defect. If the ratio of correlation length to defect length exceeds a critical value, which we determine, there is an explicit dependence of the scattering results on correlation length, and we modify the modelling to find this dependence. The modelling is cross-correlated against Monte Carlo simulations of many different surface profiles, sharing the same statistical parameter values, using numerical simulation via ray models (KA) and finite element (FE) methods accelerated with a GPU implementation. Additionally we provide experimental validations that demonstrate the accuracy of our predictions.

Keywords: Elastic shear waves, randomly rough surface, Kirchhoff approximation, stationary phase, Non-destructive evaluation, correlation length

---

*Corresponding author
Email address:* `maefanshi@ust.hk` (Fan Shi)

1. Introduction

The scattering of elastic waves in solids is well known to be affected by surface roughness [1]. The changes in scattering amplitude and intensity, and their angular distribution, are generally considered to be surface- and frequency-specific. Every rough surface is different, and can be viewed as a randomly generated dataset so scattering characteristics differ from one surface to the next. The fundamental problem must therefore be addressed using statistical techniques. Understanding the statistical scattering of elastic waves from rough surfaces is a ubiquitous problem for a wide range of applications in solid mechanics; examples include the reflection of seismic waves from irregular, or rough, interfaces to improve oil/gas exploration and productions [2], ultra-high frequency phonon reflection/transmission across an irregular solid-solid interface with continuous approximations in physics [3, 4], biomedical ultrasound measurements of an artificial bone joint [5], possible ultrasonic approaches to measure roughness or textures of contacting surfaces in tribology [6].

We are interested in providing an expected value for the scattering of ultrasound by a rough defect, such as a thermal fatigue or stress-corrosion crack, primarily for applications in NDE, but as noted above there are wider applications. Although it is not possible to predict the specific geometry of a crack, the statistics of its surface roughness may be anticipated from industrial databases of cracks formed within certain environments. A statistical expectation of the subsequent scattering intensity is then used to justify an expected sensitivity threshold for an ultrasonic inspection [7].

The scattered field is often expressed as the sum of the coherent (broadly speaking, scattering in the specular direction) and the diffuse (wide angular spread) parts. As explained by [8], early investigations centred on predicting the coherent scattering intensity [9]. For the case of a Gaussian distribution of roughness, a simple expression was derived:

$$
\begin{aligned}
I^{\mathrm{c}} &= I^{\mathrm{fs}} \exp\left(-g_{\alpha\beta}\right), \quad \alpha, \beta = \mathrm{p \ or \ s} \\
g_{\alpha\beta} &= (k_\alpha \cos\theta_i + k_\beta \cos\theta_s)^2 \sigma^2,
\end{aligned}
\tag{1}
$$

where I^{fs} is the scattering intensity from a flat surface (of the same dimension as the rough surfaces under consideration) and α, β denote the wave-type (longitudinal, p, or shear, s) for, respectively, the incident and scattered fields, whose angles are given by θ_i, θ_s as shown in Figure 1. The wavenumbers for the incident and scattered waves are $k_{\alpha|\beta}$, with unit vectors defined as:

$$
\hat{\boldsymbol{k}}_i = (\sin\theta_i, -\cos\theta_i), \quad \hat{\boldsymbol{k}}_s = (\sin\theta_s, \cos\theta_s).
\tag{2}
$$

Rough surfaces are typically characterised by two statistical parameters [1]: the standard deviation of height σ, and the lateral correlation length λ_0. These parameters are shown in Figure 1 and they are defined
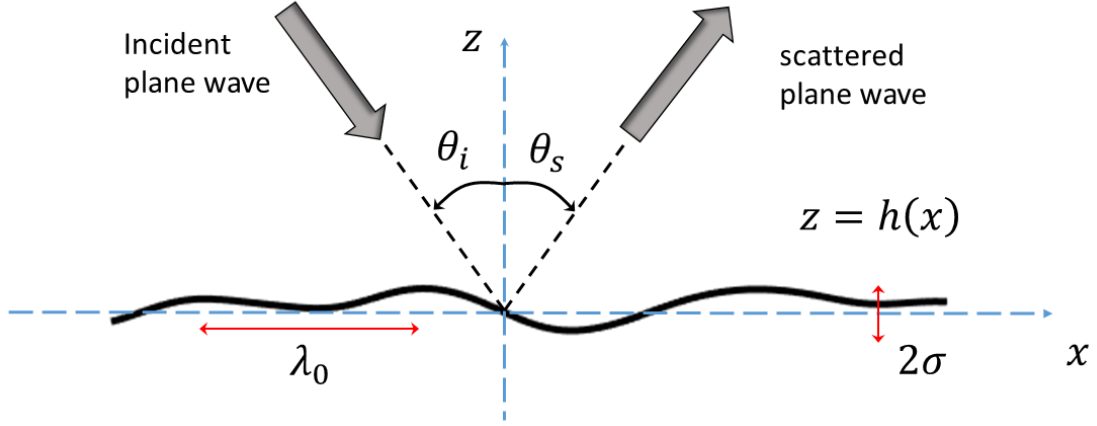
Figure 1: A plane wave scattered by a rough surface in 2D with global incident and scattering angles θ_i, θ_s. The height data of the surface is defined by $z = h(x)$, λ_0 is the correlation length and σ is the RMS height (see equations (3)).

as follows:

$$\sigma = \sqrt{< h^2 >}, \qquad < h > = \int_{-\infty}^{\infty} h p(h) \mathrm{d}h = 0, \quad \text{where } p(h) = \frac{1}{\sigma\sqrt{2\pi}} \exp\left(-\frac{h^2}{2\sigma^2}\right),$$

$$C(R) = \frac{< h(x)h(x+R) >}{\sigma^2} = \exp\left(-\frac{R^2}{\lambda_0^2}\right), \tag{3}$$

where R is the distance between any two points on the surface.

It can be seen from equation (1) that the coherent intensity depends on the RMS height σ, but not on the correlation length λ_0. The term I^{fs} is calculated using the integral formula for the far field approximation [10], or numerically, using Kirchhoff approximation (KA) discretisation. The corresponding numerical value for the theoretical ensemble average I^{c} is calculated by determining the sample average of the scattering amplitude, in the specular direction, over a large number of surface realisations.

The result (1) is widely used in industry for the justification of inspections of safety-critical components in the nuclear sector [7]. For total independence of correlation length, implied when implementing solely the formula (1), the rough surface is of infinite length. This assumption is valid for sufficiently small λ_0 such that the ratio $L/\lambda_0 \gg 1$, and when the roughness σ is also low. However, as outlined by [7, 8], for the range of length and roughness of defects commonly considered, this approach is overly conservative [9], with the diffuse field becoming increasingly important for higher levels of roughness and in off-specular directions.

To reduce the aforementioned conservatism when qualifying industrial inspections, it is highly desirable to develop a method to estimate the diffuse contribution to the total scattered field for specified roughness and scattering angles. The recent publications [8, 4] present a stochastic method to calculate the expected value of the diffuse intensity with the aid of the Kirchhoff approximation and the stationary phase method,

3

by taking the elastic wave mode conversion into consideration. For longitudinal incidence, the theoretical predictions were found to be very accurate upon validation against Monte Carlo simulations and experiments. The scattering of longitudinal waves by randomly rough surfaces has also been investigated using various sophisticated numerical methods by [11, 12, 13, 7].

The extension of the same statistical approach [8] to shear wave incidence is far from straightforward, but critical for practical NDE applications [14, 15]. Firstly, the range of validity of KA is much smaller for shear, rather than longitudinal, wave incidence as explained by [16]. KA validity breaks down at half the roughness (in terms of units of incident wavelength) due to multiple scattering and surface wave mode conversions that do not arise for analogous longitudinal cases. For this reason, the effect of correlation length is more pronounced for the shear case, since for crack dimensions and incident frequencies of practical interest in NDE, values of $\lambda_0 \leq \lambda_s/2$ remain in the KA validity range only for low values of σ. Thus, correlation lengths longer than those considered by [17, 8] must be investigated. The increase in λ_0 reduces the ratio L/λ_0, which results in a correction to the conventional derivation of the ensemble averaging. These issues are explained and addressed in what follows. Secondly, the critical angle for shear-longitudinal mode conversion [18] contributes a singularity in the derivation of the stationary phase integral for the evaluation of the diffuse field, and this is also addressed.

The stochastic model developed here to calculate expected scattering for shear wave incidence is validated against sample averaging from Monte Carlo simulations of large numbers of different surface profiles using FE methods. Confidence bands of two standard deviations show a substantial improvement on the conservative estimates [1] presently implemented within industry. Experimental validations are also provided here as further supporting evidence for the outlined techniques.

The article is organised as follows: Section 2 reviews the KA method applied to 2D randomly rough surfaces, followed by the derivation of the stationary phase approximation for shear wave incidence to obtain formulae for ensemble averages of the scattering intensities. Section 3 discusses the impact of long correlation lengths on applications of the method to NDE, and includes the correction required for both shear and longitudinal wave incidence. Section 4 presents the results of Monte Carlo simulations using numerical and FE to validate the stationary phase formulae and experimental validations are provided in Section 5, with the agreement shown to be excellent. Concluding remarks and the future outlook for the method are drawn together in Section 6.

2. Kirchhoff approximation

Kirchhoff approximation (KA) theory assumes that the motion of a single surface point is the same as if it were part of an infinite tangential plane. A plane wave incident upon each point is then assumed to undergo specular reflection, as illustrated in Figure 2 for the case of shear wave incidence. The discretisation of a
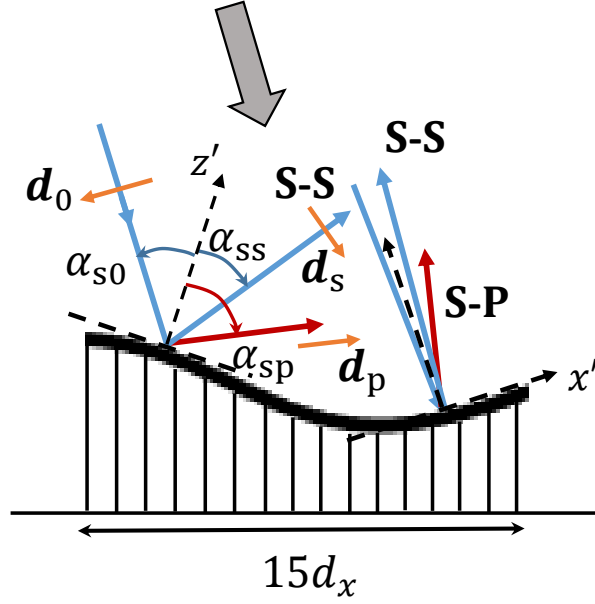
4

Figure 2: Illustration of KA discretisation for SV-incidence, facets of length d_x. Shear-shear (S-S) and shear-longitudinal (S-P) wave directions and polarisation vectors are shown, and local coordinates for each facet, x', z'.

surface into a sufficiently large number of facets, of sufficiently small dimension, and the subsequent numerical integration provide a good approximation to the total scattered field subject to certain assumptions. First order KA does not include multiple scattering effects, surface wave mode conversion and tip diffraction effects [1].

The total displacement at a facet centre is approximated as a summation of the incident shear vertical (SV) wave and the reflected shear-shear (S-S) and shear-longitudinal (S-P) waves:

$$\boldsymbol{u}^{\text{KA}} = A^{\text{SV}}\left(\boldsymbol{d}_0 + r_{\text{ss}}\,\boldsymbol{d}_{\text{s}} + r_{\text{sp}}\,\boldsymbol{d}_{\text{p}}\right), \tag{4}$$

where the vectors $\boldsymbol{d}_0, \boldsymbol{d}_{\text{s}}, \boldsymbol{d}_{\text{p}}$ are the displacement polarisation vectors and $r_{\text{ss}}, r_{\text{sp}}$ are reflection coefficients of S and P waves respectively. SV-wave incidence means that the shear wave polarisation vector is in-plane, and perpendicular to the directional vector, as indicated by the arrows in Figure 2. The term A^{SV} accounts for the change of sign of the local polarisation vector's direction, which may occur for shear, but not longitudinal, incidence [19].

2.1. Reflection coefficients

The local reflection coefficients $r_{\text{ss}}, r_{\text{sp}}$ are derived following [18], assuming a traction-free boundary condition on the boundary $z' = 0$ of a local coordinate system for each facet, and therefore, each tangential plane (see Figure 2). Thus, the coefficients depend on the local scattering angles and the wavenumbers

$k_\mathrm{s}, k_\mathrm{p}$:

$$r_\mathrm{ss} = \frac{\sin 2\alpha_\mathrm{s0} \sin 2\alpha_\mathrm{sp} - \kappa^2 \cos^2 2\alpha_\mathrm{s0}}{\sin 2\alpha_\mathrm{s0} \sin 2\alpha_\mathrm{sp} + \kappa^2 \cos^2 2\alpha_\mathrm{s0}}; \; r_\mathrm{sp} = \frac{-\kappa \sin 4\alpha_\mathrm{s0}}{\sin 2\alpha_\mathrm{s0} \sin 2\alpha_\mathrm{sp} + \kappa^2 \cos^2 2\alpha_\mathrm{s0}}, \tag{5}$$

where κ is the ratio of shear to longitudinal wavenumbers, and note that $\alpha_\mathrm{ss} = \alpha_\mathrm{s0}$ for locally specular scattering.

There is an important difference between the incident shear and incident longitudinal cases for the mode-converted waves [16]. In the former case, the reflected angle α_sp, becomes complex once a critical angle is passed:

$$\frac{\sin \alpha_\mathrm{s0}}{\sin \alpha_\mathrm{sp}} = \frac{1}{\kappa}; \quad \kappa = \frac{k_\mathrm{s}}{k_\mathrm{p}} > 1, \tag{6}$$

with the critical incident angle $\alpha_\mathrm{s0} = \alpha_\mathrm{crit}$ defined by

$$\alpha_\mathrm{crit} = \sin^{-1}\left(\frac{1}{\kappa}\right). \tag{7}$$

The analogous longitudinal-shear mode conversion shares a similar condition to (6), but with the reciprocal ratio of sines, ensuring that α_ps is always real.

2.2. Formulation of scattering problem

The total displacement field is given by

$$\boldsymbol{u} = \boldsymbol{u}^\mathrm{sc} + \boldsymbol{u}^\mathrm{inc},$$

with the scattered field represented by the elastodynamic Helmholtz integral formula [1, 8, 20]:

$$u_k^\mathrm{sc}(\boldsymbol{R}) = \int_{\mathcal{S}(\boldsymbol{r})} \Sigma_{ijk}(|\boldsymbol{R} - \boldsymbol{r}|)\, u_i^\mathrm{KA}(\boldsymbol{r}) n_j(\boldsymbol{r})\, d\mathcal{S}(\boldsymbol{r}), \tag{8}$$

where Σ_{ijk} is Green's stress tensor, $\boldsymbol{R}$ is the location of the observation point, $\boldsymbol{r}$ is a point on the rough surface $\mathcal{S}(\boldsymbol{r})$, $\boldsymbol{n}$ is the outward unit normal and $u_i^\mathrm{KA}(\boldsymbol{r})$ is the ith component of the KA boundary displacement (4). Note that since we are considering 2D, the $k = 2$ component of scattered displacement u_k^sc is zero and the dummy indices $i, j \neq 2$ with the index values 1 and 3 corresponding to the x and z directions respectively (see Figure 1).

The Green's stress tensor can be expressed explicitly as [21]:

$$\Sigma_{ij;k}^G(|\boldsymbol{R} - \boldsymbol{r}|) = (1 - 2k_p^2/k_s^2) G(k_p|\boldsymbol{R} - \boldsymbol{r}|)_{,k} \delta_{ij} - \frac{2}{k_s^2}[G(k_p|\boldsymbol{R} - \boldsymbol{r}|) - G(k_s|\boldsymbol{R} - \boldsymbol{r}|)]_{,ijk}$$
$$+ G(k_s|\boldsymbol{R} - \boldsymbol{r}|)_{,j}\delta_{ik} + G(k_s|\boldsymbol{R} - \boldsymbol{r}|)_{,i}\delta_{jk} \tag{9}$$

where k_p and k_s are the compressional and shear wavenumber. The notation $f_{,i} = \frac{\partial f}{\partial x_i}$ is used here, and δ refers to the Dirac delta function. The function $G(k_\beta|\boldsymbol{R} - \boldsymbol{r}|)$ is the acoustic Green's function, which in 2D is expressed as:

$$G(k_\beta|\boldsymbol{R} - \boldsymbol{r}|) = -\frac{i}{4} H_0^{(1)}(k_\beta|\boldsymbol{R} - \boldsymbol{r}|) \tag{10}$$

6

Here $H_0^{(1)}(k_\beta|\boldsymbol{R} - \boldsymbol{r}|)$ denotes the zero order Hankel function of the first kind.

Using far-field assumptions [19] $R \gg r$ and $k_\mathrm{s}R \gg 1$, and $|\boldsymbol{R} - \boldsymbol{r}| \approx R - \hat{\boldsymbol{R}} \cdot \boldsymbol{r}$ [4] where $\hat{\boldsymbol{R}}$ is the unit vector in the direction of $\boldsymbol{R}$, the integral (8) simplifies to

$$\boldsymbol{u}^{\mathrm{sc}}(\boldsymbol{R}) = -\mathrm{i}k_\beta \sqrt{\frac{2\pi\mathrm{i}}{k_\beta}} \frac{e^{\mathrm{i}k_\beta R}}{2\pi\sqrt{R}} \sum_{\beta=\mathrm{p,s}} \int_{\mathcal{S}_0} \boldsymbol{F}_{\mathrm{s}\beta}(\kappa, \boldsymbol{R}) e^{\mathrm{i}k_\beta \phi_{\alpha\beta}} \, d\mathcal{S}_0. \tag{11}$$

Here, the term $\boldsymbol{F}_{\mathrm{s}\beta}$ represents the boundary displacement where the index β denotes the scattered wave-type, which is shear, s, or longitudinal, p:

$$\boldsymbol{F}_{\mathrm{sp}}(\kappa, \boldsymbol{R}) = \left[(\boldsymbol{u}^{\mathrm{KA}} \cdot \boldsymbol{N}) \left(1 - \frac{2}{\kappa^2} \right) + \frac{2}{\kappa^2} \left(\boldsymbol{u}^{\mathrm{KA}} \cdot \hat{\boldsymbol{R}} \right) \left(\boldsymbol{N} \cdot \hat{\boldsymbol{R}} \right) \right] \hat{\boldsymbol{R}} \tag{12}$$

$$\boldsymbol{F}_{\mathrm{ss}}(\kappa, \boldsymbol{R}) = \left(\boldsymbol{N} \cdot \hat{\boldsymbol{R}} \right) \boldsymbol{u}^{\mathrm{KA}} + \left(\boldsymbol{u}^{\mathrm{KA}} \cdot \hat{\boldsymbol{R}} \right) \boldsymbol{N} - 2 \left(\boldsymbol{u}^{\mathrm{KA}} \cdot \hat{\boldsymbol{R}} \right) \left(\boldsymbol{N} \cdot \hat{\boldsymbol{R}} \right) \hat{\boldsymbol{R}}. \tag{13}$$

Note that the integral (11) has been transferred to one along the mean plane, $\mathcal{S}_0$, of the surface, and that $\boldsymbol{N}$ is the unnormalised vector normal to the surface, defined by $(-\partial h/\partial x, 1)$. We also clarify that the notation $\boldsymbol{F}_{\mathrm{s}\beta}$ has been adopted to anticipate the relationship $2\boldsymbol{F}_{\mathrm{s}\beta} = \boldsymbol{U}_{\mathrm{s}\beta}$ used in previous publications [8, 4] which followed the optical designation [22]. The constant in (11) has been adjusted to maintain consistency with the previous work.

Equation (11) contains the phase term $\phi_{\alpha\beta}$, which is defined in the following way:

$$\begin{aligned} \phi_{\alpha\beta} &= \quad A_{\alpha\beta}x + C_{\alpha\beta}h(x), \\ A_{\alpha\beta} &= \quad \frac{k_\alpha}{k_\beta}\sin\theta_i - \sin\theta_s, \\ C_{\alpha\beta} &= -\left(\frac{k_\alpha}{k_\beta}\cos\theta_i + \cos\theta_s \right). \end{aligned} \tag{14}$$

The local nature of the rough surface is incorporated via the variation in height $h(x)$, the local normal $\boldsymbol{N}$ and the local boundary displacement $\boldsymbol{u}^{\mathrm{KA}}$.

It is not possible to simplify (11) in its present form, owing to the dependence of the surface slope on local surface-specific parameters. However, by assuming that specular points are of stationary phase [4], and provide the major contribution to the scattered field, an analytic expression can be derived to approximate the total scattered intensity. This expected value for scattering depends only on the incident frequency and the statistical characterisation of a surface, i.e. σ and λ_0, and and not on specific surface geometry.

2.3. Specular points and stationary phase method

The concept of using specular points to approximate scattering effects originates from the optical community [23, 24]. For a given global scattering angle θ_s (see Figure 1), specular points indicate those locations where the local surface normal is such that the local specular scattering direction is parallel to the global

direction θ_s. Such points are identified by applying a stationary phase approach [8], since the elastodynamic term $\boldsymbol{F}_{\text{s}\beta}$ is a slowly varying function relative to the phase $\phi_{\alpha\beta}$; the first-order derivatives with respect to x are set to zero (see equation (14)):

$$\frac{\partial h}{\partial x} = -\frac{A_{\alpha\beta}}{C_{\alpha\beta}}. \tag{15}$$

It can be seen from equations (14),(15) that the surface slopes are approximated as constants for given incident/scattering angles, wave-types and material properties. The number of times a constant line intersects the actual slope values for a specific rough surface indicates the number of specular points, and the quality of the approximation, as illustrated in Figure 3.
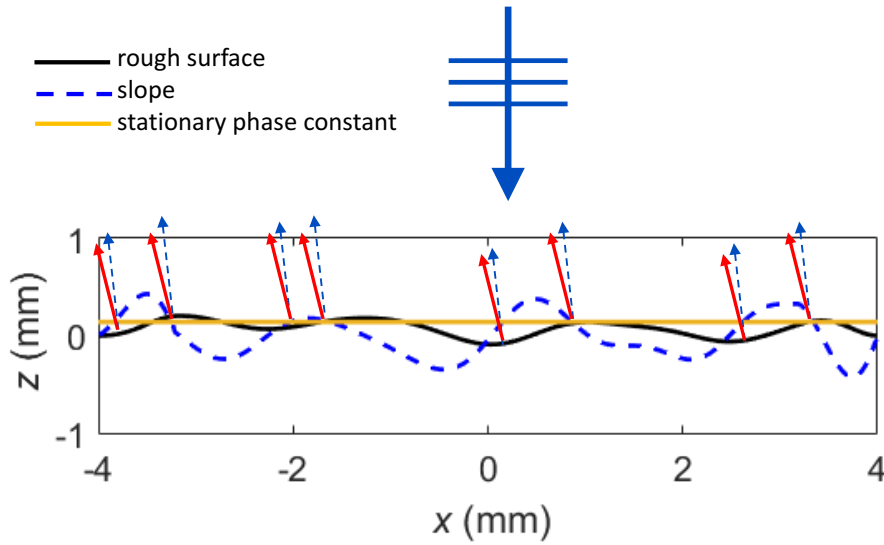
Figure 3: Stationary phase concept and specular points for a rough surface (solid curve). Local surface normals and specular directions are denoted by, respectively, dashed and solid arrows. The dimensionless slopes of the rough surface (dashed curve) and the stationary phase approximation (straight line) for $\theta_i = 0°, \theta_s = -16°$ are added for the sake of illustration.

A Gaussian rough surface characterised by $\lambda_0 = \lambda_s$, $\sigma = \lambda_s/6$ is insonified by a normally incident plane shear wave in Figure 3. The surface itself is shown by the solid curve, and for illustrative purposes, the first order approximation to its slope by the dashed curve. For a specific frequency and scattered angle, $\theta_s = -16°$ say, equation (15) determines the constant which is used by the stationary phase method to approximate the slope. We have added a straight line at this value to Figure 3 to indicate the number of points on the surface for which the stationary phase constant coincides with the real slope values.

The intersections of this line and the slope curve give the stationary points, where the local surface normals (dashed arrows) are such that the specular scattering direction coincides with the global angle $\theta_s = -16°$. Thus, for a range of scattering angles, $-60° \leq \theta_s \leq 60°$, substitution of equation (15) into equations (12),(13) yields x- and z- components for $\boldsymbol{F}_{\text{s}\beta}$, which can be plotted versus θ_s. A similar approach

8

is adopted for longitudinal incidence [8] to obtain $\boldsymbol{F}_{p\beta}$.

The evaluation of these constants is independent of roughness and for three of the four mode-types, i.e. P-P, P-S and S-P, produces real values. However, for the S-S case, the existence of the critical incident angle α_{crit} (7), means that for a range of θ_s, the local reflection coefficients become complex. These coefficients are relevant via the Kirchhoff representation (4), which is present in (12),(13). It is simple to show that the range of affected θ_s is given by

$$\theta_s > 2\alpha_{\text{crit}} - \theta_i. \tag{16}$$

For $\theta_s = 2\alpha_{\text{crit}} - \theta_i$, the local specular scattering direction for the S-P mode is parallel to the surface, i.e. $90°$, as surface wave mode conversion takes place [18], p.179.

It may seem counter-intuitive that the effect of critical angle arises only for S-S waves in the stationary phase approach, not the S-P case. Equations (14), (15) provide the explanation, since the approximation to the normal substituted into (12)-(13) depends on the ratio $A_{\alpha\beta}/C_{\alpha\beta}$, and for S-P waves, this ratio is above the threshold for all values of θ_s. However, for the S-S case, for $\theta_s > 2\alpha_{\text{crit}} - \theta_i$, the ratio $A_{\alpha\beta}/C_{\alpha\beta}$ becomes sufficiently negative such that the local normal approximation enforces surface wave mode-conversion of the S-P wave. All subsequent associated angles α_{sp} become complex, as do the reflection coefficients, originally defined by (5), but subsequently adjusted as (17):

$$r_{\text{ss}} = -\exp(-2\mathrm{i}\xi);$$
$$r_{\text{sp}} = \frac{\exp(-\mathrm{i}\xi + \tau k_{\text{s}})\sin 4\alpha_{\text{s0}}}{\sqrt{\kappa^2 \cos^4(2\alpha_{\text{s0}}) + 4(\kappa^2 \sin^2(\alpha_{\text{s0}}) - 1)\sin^2(2\alpha_{\text{s0}})\sin^2(\alpha_{\text{s0}})}}, \tag{17}$$

where the parameters ξ, τ are introduced for complex α_{sp}, with the polarisation vector $\boldsymbol{d}_{\text{p}}$ in (4) changed accordingly, with $\gamma = \arg(\alpha_{\text{sp}})$:

$$\tan\xi = \frac{2\sqrt{(\kappa^2 \sin^2 \alpha_{\text{s0}} - 1)}\sin 2\alpha_{\text{s0}} \sin \alpha_{\text{s0}}}{\kappa \cos^2 2\alpha_{\text{s0}}},$$
$$\tau = \frac{\sinh\gamma}{\sqrt{\sinh^2\gamma + \cosh^2\gamma}}. \tag{18}$$

The impact of the critical angle is illustrated in Figure 4. In Figure 4(a), the x- and z-components of $\boldsymbol{F}_{\text{ss}}$ are plotted using both equations (5) (dashed and dotted curves) and equations (17) (solid blue and red curves) for $\theta_i = 15°$ and over much of the range the solid and dashed/dotted curves are indistinguishable. The extreme effect on $\boldsymbol{F}_{\text{ss}}$ for $\theta_s > 2\alpha_{\text{crit}} - \theta_i \simeq 48.3°$ is clear, as is the improvement by adjusting the reflection coefficients. The associated impact on the diffuse intensity (derived in the next section) is also evident in Figure 4(b), where the dot-dashed curve shows the uncorrected result, with the solid curve indicating the adjusted result. The singularity marking the vicinity of the surface wave conversion is clearly seen, but for subsequent values of θ_s the adjusted stationary phase value matches the Monte Carlo (MC) numerical result (dot-dashed). Note from the inset in Figure 4(b) that the singular behaviour, which is a marker for
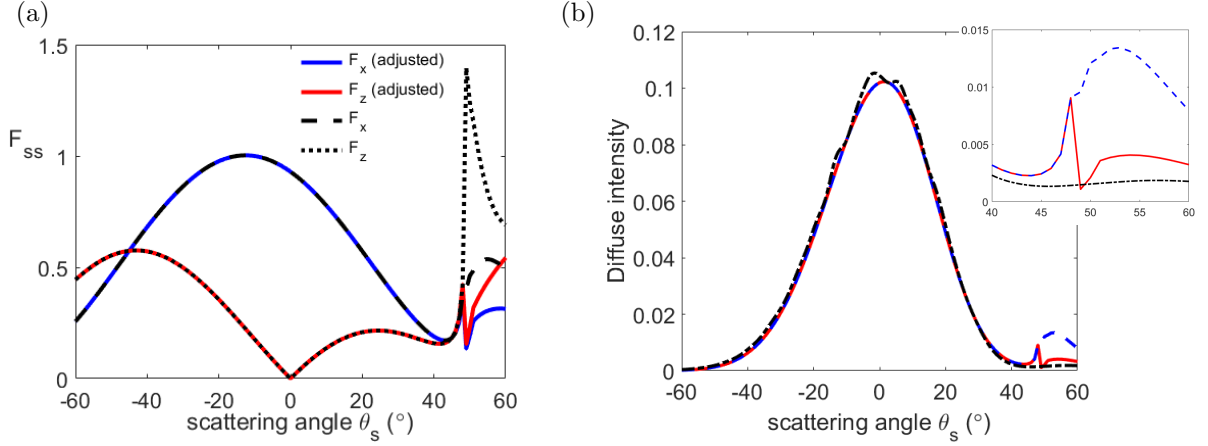
9

Figure 4: Critical angles for shear wave incidence. (a) Elastodynamic term $\boldsymbol{F}_{\text{ss}}$ plotted versus θ_s. Solid (adjusted) and dashed curve pair represents the x-component and solid (adjusted) and dotted pair represents the z-component. (b) Diffuse intensity plotted versus θ_s for $\theta_i = 15°$ for $\lambda_0 = \lambda_{\text{s}}, \sigma = \lambda_{\text{s}}/6, R = 50\text{mm}$. Dot-dashed is the MC result, dashed is uncorrected stationary phase and solid is adjusted stationary phase, all clearly visible around $\theta_s = 2\alpha_{\text{crit}} - \theta_i$ in the inset.

the mode conversion, initiates just below the critical angle at around $\theta_s = 45°$. This is consistent with the observation by Harker [25] p.30, who noted the marked dip in the reflected shear wave amplitude prior to the critical angle for SV-waves reflected by a traction-free boundary.

From a practical point of view, the impact of the critical angle on the stationary phase approach for shear wave incidence is negligible for ultrasonic inspection of defects, since the preferred choices of incident angle, for example $\theta_i = 45°$ [15, 26], are selected with the critical angle in mind. As stated by [15], it is common to operate within the range $32° < \theta_i < 58°$ for angled shear wave pulse-echo contact inspection set-ups [26], since it is beyond the first critical angle for steel such that only shear waves propagate within the component under inspection. Other important set-ups are designed for head-on incidence with respect to the defect surface, i.e. low values of θ_i for which the range of affected scattering angles is small and distant from both the specular direction, and peak of the diffuse field. However, for incident angles around α_{crit} which are avoided in practice due to surface wave mode conversions, the specular scattered direction coincides with the critical value of $\theta_s = 2\alpha_{\text{crit}} - \theta_i$ whereby the stationary phase and KA theories become unreliable.

2.4. Diffuse intensity

The motivation for applying a stationary phase approach is to remove the derived constant term $\boldsymbol{F}_{\text{s}\beta}$ from the integrand in (11) by substituting the expression (15) into (12),(13), obtaining:

$$\boldsymbol{u}^{\text{sc}}(\boldsymbol{R}) = -\mathrm{i}k_\beta \sqrt{\frac{2\pi\mathrm{i}}{k_\beta}} \frac{e^{\mathrm{i}k_\beta R}}{2\pi\sqrt{R}} \sum_{\beta=\text{p,s}} \boldsymbol{F}_{\text{s}\beta} \bigg|_{\boldsymbol{N}=\left(-\frac{A_{\text{s}\beta}}{C_{\text{s}\beta}},1\right)} \int_{\mathcal{S}_0} e^{\mathrm{i}k_\beta \phi_{\text{s}\beta}} \, d\mathcal{S}_0, \tag{19}$$

10

for shear-wave incidence. The equivalent expression for longitudinal incidence was derived by [8, 4]. Thus, the integrand in (19) no longer depends on the surface slope, but only on the frequency and height function $h(x)$. This allows one to derive the ensemble average formulae for scattering intensity:

$$I^{\mathrm{t}} = \langle \boldsymbol{u}^{\mathrm{sc}} \bar{\boldsymbol{u}}^{\mathrm{sc}} \rangle = I^{\mathrm{c}} + I^{\mathrm{d}}, \tag{20}$$

where the superscripts t, c, d denote the total, coherent and diffuse parts, respectively.

The formula for the coherent intensity was presented earlier in equation (1). The dominant component
of I^{d} depends on the wave-type. Broadly speaking, longitudinal waves will possess a dominant z-component of I^{d}, and the shear wave I^{d} will be dominated by its x-component, provided that $\theta_i \ll 45°$. The method to calculate either component is identical and involves assuming two arbitrary points on the rough surface (x_0, h_0) and (x_1, h_1).

As first defined by [1], the average diffuse intensity can be written in the form:

$$I^{\mathrm{d}} = \langle \boldsymbol{u}^{\mathrm{sc}} \bar{\boldsymbol{u}}^{\mathrm{sc}} \rangle - \langle \boldsymbol{u}^{\mathrm{sc}} \rangle \langle \bar{\boldsymbol{u}}^{\mathrm{sc}} \rangle. \tag{21}$$

Using the arbitrary points defined above, and equation (19), we obtain

$$I^{\mathrm{d}} = \frac{k_\beta F_{\mathrm{s}\beta}^2}{2\pi R} \int_{-L/2}^{L/2} \int_{-L/2}^{L/2} e^{\mathrm{i}k_\beta A_\beta(x_0 - x_1)} \left(\left\langle e^{\mathrm{i}k_\beta C_\beta(h_0 - h_1)} \right\rangle - \left\langle e^{\mathrm{i}k_\beta C_\beta h_0} \right\rangle \left\langle e^{-\mathrm{i}k_\beta C_\beta h_1} \right\rangle \right) dx_0 dx_1. \tag{22}$$

Note that for the sake of brevity, we have omitted the subscript s, indicating shear incidence, for the terms $A_{\alpha\beta}, C_{\alpha\beta}$.

We make the change of variables $\Delta x_1 = x_1 - x_0$ and define the two-dimensional characteristic function χ_2 in the following way:

$$\left\langle e^{\mathrm{i}k_\beta C_\beta(h_0 - h_1)} \right\rangle = \chi_2(k_\beta C_\beta, -k_\beta C_\beta, \Delta x_1) = \exp\{-g_\beta[1 - W(\Delta x_1)]\}. \tag{23}$$

The definition of χ_2 is determined by the height distribution under consideration; for the Gaussian case considered here, χ_2 has the analytical form (23) [4] and, when $\Delta x_1 \gg \lambda_0$, has the property [1]:

$$\lim_{\Delta x_1 \to 0} \chi_2(k_\beta C_\beta, -k_\beta C_\beta, \Delta x_1) - \chi(k_\beta C_\beta)\bar{\chi}(k_\beta C_\beta) \to 0. \tag{24}$$

Here we also define the following functions:

$$
\begin{aligned}
W(\Delta x_1) &= \exp\left[-\left(\frac{\Delta x}{\lambda_0}\right)^2\right] \\
\chi(k_\beta C_\beta) &= \left\langle e^{\mathrm{i}k_\beta C_\beta h_0} \right\rangle = \exp\left(-\frac{k_\beta^2 C_\beta^2 \sigma^2}{2}\right) = \exp(-g_\beta/2) = \left\langle e^{-\mathrm{i}k_\beta C_\beta h_1} \right\rangle = \bar{\chi}(k_\beta C_\beta),
\end{aligned}
\tag{25}
$$

noting that the second term of (24) is equal to $\exp(-g_\beta)$, the importance of which will be explained below.

11

Equation (22) then becomes

$$I^{\mathrm{d}} = \frac{k_\beta F_{\mathrm{s}\beta}^2}{2\pi R} \int_{-L/2}^{L/2} \int_{-L/2}^{L/2} e^{\mathrm{i}k_\beta A_\beta \Delta x_1} [\chi_2(k_\beta C_\beta, -k_\beta C_\beta, \Delta x_1) - \chi(k_\beta C_\beta)\bar{\chi}(k_\beta C_\beta)] dx_1 d\Delta x_1 \tag{26}$$
$$= \frac{k_\beta F_{\mathrm{s}\beta}^2}{2\pi R} L \int_{-\infty}^{\infty} e^{\mathrm{i}k_\beta A_\beta \Delta x_1} [\chi_2(k_\beta C_\beta, -k_\beta C_\beta, \Delta x_1) - \chi(k_\beta C_\beta)\bar{\chi}(k_\beta C_\beta)] d\Delta x_1,$$

where L is the finite length of the crack, but we have assumed that the limits of the integral are extended from $\pm L/2$ to $\pm\infty$, under the condition that L, and therefore $\max(|\Delta x_1|)$, is much larger than λ_0 so that the condition (24) holds. Physically, for points on the surface with large separation, the function $\chi_2 - \chi\bar{\chi}$ (and therefore the integrand in (26)) is sufficiently small to be negligible. The assumption of infinite limits is an important step in deriving the analytical formula for the expected intensity, since it allows the use of a Gaussian integral substitution in what follows.

Referring to the expression for χ_2 (23), we use the Taylor expansion to approximate $\exp\{g_\beta W(\Delta x_1)\}$:

$$e^{g_\beta W(\Delta x_1)} = \sum_{n=0}^{\infty} \frac{k_\beta^{2n} C_\beta^{2n} \sigma^{2n} [W(\Delta x_1)]^n}{n!}, \tag{27}$$

noting that the $n = 0$ term is 1. Thus, the substitution of the Taylor series (27) into (26) leads to:

$$I^{\mathrm{d}} = \frac{k_\beta F_{\mathrm{s}\beta}^2}{2\pi R} L e^{-g_\beta} \int_{-\infty}^{\infty} e^{\mathrm{i}k_\beta A_\beta \Delta x_1} \sum_{n=1}^{\infty} \frac{k_\beta^{2n} C_\beta^{2n} \sigma^{2n} e^{-n\Delta x_1^2/\lambda_0^2}}{n!} d\Delta x_1. \tag{28}$$

Note that the sum in (28) starts from $n = 1$, since the $n = 0$ term cancels the coherent contribution $\chi(k_\beta C_\beta)\bar{\chi}(k_\beta C_\beta) = e^{-g_\beta}$. Additionally in expression (28), we have removed the term e^{-g_β} from within the integral, since it has no dependence on Δx_1. Swapping the order of the integral and sum, and completing the square of the integrand, results in a simple Gaussian integral which is solved analytically:

$$I^{\mathrm{d}} = \frac{k_\beta F_{\mathrm{s}\beta}^2 L \lambda_0 \sqrt{\pi} e^{-g_\beta}}{2\pi R} \sum_{n=1}^{\infty} \frac{g_\beta^n}{n! \sqrt{n}} \exp\left[-\frac{k_\beta^2 A_\beta^2 \lambda_0^2}{4n}\right]. \tag{29}$$

This result is similar to the longitudinal result derived in [4] but for shear incidence, there are differences related to the critical angle and a reduced range of validity. The reason is that KA theory breaks down for shear incidence for short correlation lengths [16]. For finite crack dimensions of practical interest, i.e. $L \leq 8$mm [15, 16], the relatively larger correlation lengths required for KA validity invalidate the important assumption $L \gg \lambda_0$ used in the derivation above to obtain the analytical formulae for total and diffuse intensities. In the next section, we explain how a correction to the formulae enables the stationary phase approach to also be used for cases of long correlation length.

3. Stationary phase approach for rough surfaces with long correlation length

It is increasingly important in industry to detect rough defects as early as possible, and of small enough size. Certain inspection configurations achieve better sensitivity for smaller cracks with shear waves rather

12

than with longitudinal waves [14, 15]. As explained by [16], KA theory has a smaller range of validity for shear wave incidence. Two of the key factors are multiple scattering and surface wave mode conversion, which are exacerbated by reduction in correlation length. For example, a rough defect of length 8mm for transducer frequency between 2 and 5MHz, is modelled reliably using KA theory for $\lambda_0 \geq \lambda_s$. In the paper [16], validity ranges were provided for various σ for $\lambda_0 = 2\lambda_s, \lambda_s$ and $\lambda_s/2$. In contrast, for longitudinal incidence, [17], values of $\lambda_0 \leq \lambda_p/4$ were considered.

3.1. Long correlation length correction term

Investigations of the stationary phase analytical formulae for diffuse intensity (29) for shear wave incidence show that the expected value predictions (29) have errors of up to 20% for cases of $\lambda_0 = 2\lambda_s$ and $\lambda_s/16 \leq \sigma \leq \lambda_s/8$ for defects whose length L is such that the ratio L/λ_0 is insufficently large. For a specific example of ferritic steel, with a frequency 5MHz and $L = 8$mm, $L/\lambda_0 \simeq 6.28$, which is insufficiently large to justify the extension of the limits of the boundary integral (26) to infinity. An example is illustrated in Figure 5(a).
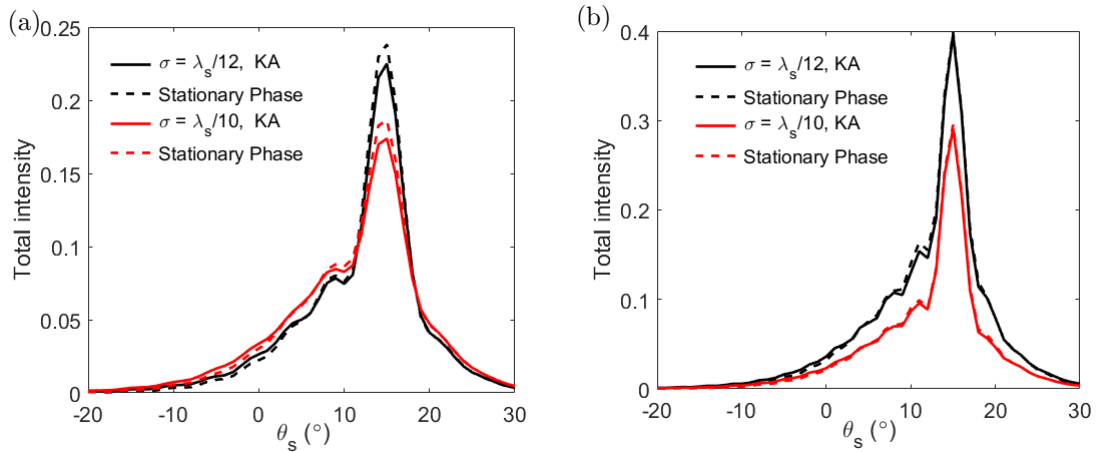
Figure 5: Normalised total intensity of S-S mode for $\theta_i = 15°$ versus scattering angle θ_s for MC KA (solid curves, $N = 4000$) and SPM (dashed curves). $R = 100$mm, frequency $= 5$MHz and $\lambda_0 = 2\lambda_s$ for two values of crack length L: (a) $L = 8$mm, (b) $L = 12$mm.

For two low values of the RMS height $\sigma = \lambda_s/12$ and $\lambda_s/10$, there are errors in the specular total intensity with the stationary phase method (SPM) overpredicting the value by 5.9% and 7.3%, respectively, as compared with the MC KA results. In contrast, for an increased value of $L = 12$mm, but all other parameters defined as in Figure 5(a), the errors are negligible as illustrated in Figure 5(b), where the ratio L/λ_0 has increased from $\simeq 6.28$ to 9.42. In Figure 5(b), the increased number of correlation lengths per unit length ensures that the condition (24) is satisfied for a sufficient number of spacings Δx_1 such that the assumption of infinite limits in the integral (26) is valid.

13

We have found from extensive numerical simulation that formula (29) works well provided that the larger values of surface point spacings Δx_1 satisfy (24). For contradictory cases, the source of error is identified by considering the integrand function $\chi_2 - \chi\bar{\chi}$ in (26), and in particular referring to its Taylor expansion form using (27):

$$\chi_2 - \chi\bar{\chi} = e^{-g_\beta} \sum_{n=0}^{\infty} \frac{k_\beta^{2n} C_\beta^{2n} \sigma^{2n} [W(\Delta x_1)]^n}{n!} - e^{-g_\beta} = e^{-g_\beta} \left(k_\beta^2 C_\beta^2 \sigma^2 e^{-\Delta x_1^2/\lambda_0^2} + \frac{k_\beta^4 C_\beta^4 \sigma^4 e^{-\Delta x_1^4/\lambda_0^4}}{2} + \dots \right).$$
(30)

Figure 6(a) illustrates the right hand side of (30) for a specific scattering direction, with the sum of the first 4 terms plotted successively using solid lines, along with the exact expression using equation (23) shown with the dashed curve.

It is clear that the Taylor series converges since the sum of the first 4 terms is very close to the true value. The other striking feature of Figure 6(a) is that only the first term (solid blue) contributes non-zero values to $\chi_2 - \chi\bar{\chi}$ for $|\Delta x_1| > 1.9$mm. As the shaded regions indicated by the solid dashed lines in Figure 6(a) show, around 12.5% of the total length is affected, such that all spacings in the range 1.9mm $< \Delta x_1 <$ 2.8mm do not satsify (24). In contrast, the second, third and fourth terms in the Taylor series are non-zero only for $\Delta x_1 < 1.9$mm (i.e. less than a quarter of the defect) and so the dominant part of the errors when using SPM for such cases are linked to the $n = 1$ term.
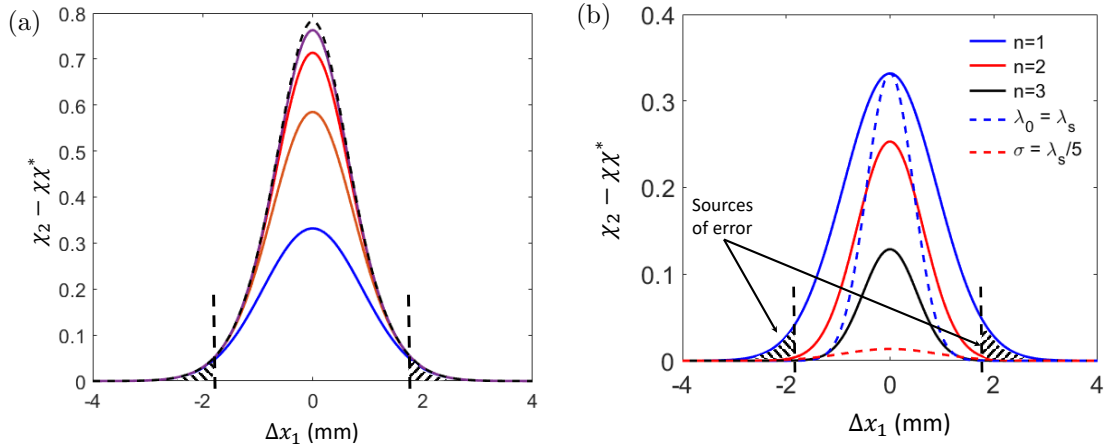

Figure 6: Integrand function $\chi_2 - \chi\bar{\chi}$ plotted versus x for a defect of length $L = 8$mm, $\lambda_0 = 2\lambda_s$, $\sigma = \lambda_s/10$, $\theta_i = 15°$, frequency = 5MHz. (a) The sums of the Taylor expansion form for $n = 1 - 4$ are plotted successively using solid curves, the true value with dashed curve. (b) The first 3 terms using the Taylor expansion are plotted using solid curves, the $n = 1$ term for $\lambda_0 = \lambda_s$ (dashed blue) and for $\sigma = \lambda_s/5$ (dashed red) are also shown.

Figure 6(b) provides additional evidence for the contributions of the Taylor series terms (solid curves) as well as the differences that arise for a reduction in λ_0 (dashed blue, $\lambda_0 = \lambda_s$) and an increase in σ (dashed red, $\sigma = \lambda_s/5$). The Taylor $n = 2$ and $n = 3$ terms produce non-zero $\chi_2 - \chi\bar{\chi}$ values for a sufficiently

14

small range and magnitude of $|\Delta x_1|$ to justify the assumption of infinite limits in (26). However, for larger spacings Δx_1, the $n = 1$ term contributes non-zero $\chi_2 - \chi\bar{\chi}$ values that are not sufficiently negligible to justify the replacement of the finite limits of Δx_1 with $\pm\infty$. For a reduction in λ_0 such that $L/\lambda_0 \simeq 12.56$ in Figure 6(b), the $n = 1$ term (shown by the dashed blue curve) no longer contributes the same error when applying SPM. Similarly, for the correlation length $\lambda_0 = 2\lambda_\mathrm{s}$ of Figure 6(a), an increase in σ to $\lambda_\mathrm{s}/5$ leads to the $n = 1$ term (dashed red curve) also no longer contributing an error.

Defining the ratio $L/2\lambda_0$ to be ζ, we prescribe the following bounding criteria for when the conventional SPM formula (29) requires correction:

$$\zeta = \frac{L}{2\lambda_0} < 4; \qquad \lambda/16 \leq \sigma \leq \lambda/8, \tag{31}$$

where λ is the incident wavelength. For smaller values of σ, the diffuse field is negligible compared with the coherent field, and for higher values of σ, the assumption of infinite limits is justified as illustrated, for example, by the dashed red curve shown in Figure 6(b). For the corrected SPM, the formula for the diffuse field (29) is used to calculate the expected diffuse intensity and then corrected by subtracting the leading order error coming from the $n = 1$ term in (30). For the range of σ affected, the term $k_\beta^2\sigma^2 = O(1)$ and we bound the exponent using $\zeta = L/2\lambda_0$, leading to:

$$\begin{aligned} I_\mathrm{corr}^\mathrm{d} &= I^\mathrm{d} - \frac{k_\beta F_{\mathrm{s}\beta}^2}{2\pi R} C_\beta^2 e^{-\zeta^2} \int_{-L/2}^{L/2} e^{\mathrm{i}k_\beta A_\beta \Delta x_1} d\Delta x_1, \\ &= I^\mathrm{d} - \frac{k_\beta F_{\mathrm{s}\beta}^2}{2\pi R} C_\beta^2 e^{-\zeta^2} L \operatorname{sinc}\left(\frac{A_\beta k_\beta L}{2}\right). \end{aligned} \tag{32}$$

Note that A_β, C_β contain information regarding the angular range and ζ carries the correction for the ratio of defect length to correlation length.

Generally, the order of the term $\exp(-\zeta^2)$ is sufficiently small for assumption (24) to hold provided that ζ (31) is sufficiently large. Physically, one can think of the surface requiring a minimum number of correlation lengths for the application of the stationary phase theory to be valid. The smaller the correlation length λ_0, the better the specular point approximation works. However, for a fixed length L, larger values of λ_0 reduce the number of peaks and troughs, which reduces the independence of neighbouring points leading to larger sections of the surface being approximated by the specular point contributions. As a result, the stationary phase theory overpredicts the diffuse field as the $L\lambda_0$ term in (29) grows with decreasing ζ.

3.2. Illustrative examples

Examples illustrating the application of the leading order error correction to the stationary phase method are shown for both shear and longitudinal incidence in Figure 7. The method for quantifying the initial error, and subsequent correction, is the MC method described in detail in our previous publications [17, 16]. For the valid range of KA, it is sufficient to compare the stationary phase formulae (29) and (32) with the KA ensemble average of a very large number, $N = 4000$ here, of rough surface realisations for specified λ_0, σ.
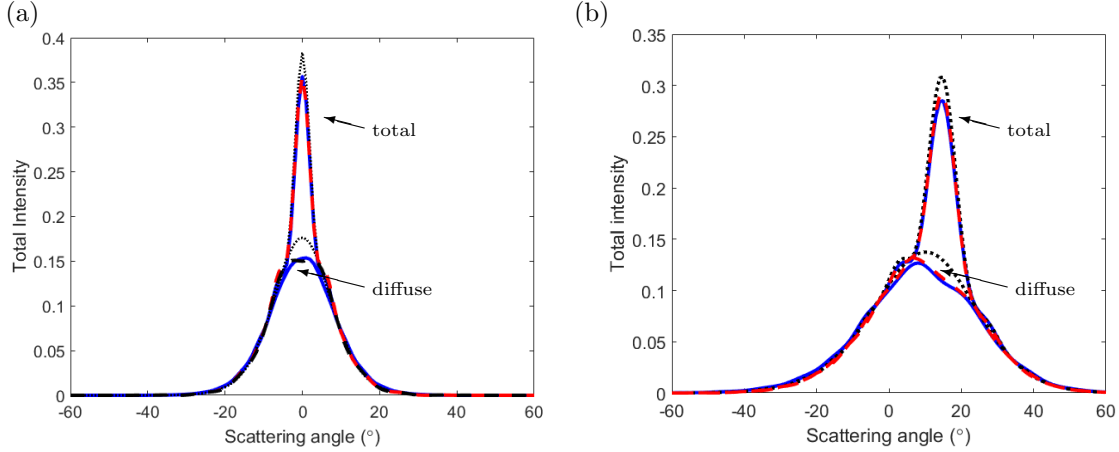
15

Figure 7: Comparison of SPM and MC KA methods ($N = 4000$) for scattering intensity for shear and longitudinal incidence. Solid curves are MC KA, dashed curves are corrected SPM and dotted curves are uncorrected SPM. (a) S-S mode for $\theta_i = 0°, \lambda_0 = 2\lambda_s, \sigma = \lambda_s/10, R = 100$mm. (b) P-P mode for $\theta_i = 15°, \lambda_0 = \lambda_p, \sigma = \lambda_p/10, R = 50$mm.

The MC KA method uses the following formulae to calculate the total and coherent intensities:

$$I_{\mathrm{KA}}^{\mathrm{t}} = \frac{1}{N} \sum_{n=1}^{N} |\boldsymbol{u}_n^{\mathrm{sc}}(\theta_s)|^2 ; \qquad I_{\mathrm{KA}}^{\mathrm{c}} = \left| \frac{1}{N} \sum_{n=1}^{N} \boldsymbol{u}_n^{\mathrm{sc}}(\theta_s) \right|^2 . \tag{33}$$

The diffuse field is the difference of the two:

$$I_{\mathrm{KA}}^{\mathrm{d}} = I_{\mathrm{KA}}^{\mathrm{t}} - I_{\mathrm{KA}}^{\mathrm{c}}. \tag{34}$$

Thus, the more reliable the MC results for $I_{\mathrm{KA}}^{\mathrm{t}}, I_{\mathrm{KA}}^{\mathrm{c}}$, the more reliable $I_{\mathrm{KA}}^{\mathrm{d}}$ is. It is therefore important to compare all three quantities with one another.

For the case of shear incidence with $\lambda_0 = 2\lambda_s, \sigma = \lambda_s/10$, frequency = 5MHz, normal incidence, $R = 100$mm and $L = 8$mm, the total and diffuse intensities are plotted versus θ_s in Figure 7(a). Normalisation with respect to the reflection from a flat surface of the same length has been performed. The solid blue curves are the MC KA results for $N = 4000$ surfaces. The dotted curves are the expected values generated using SPM formulae (29), and the dashed curves are the results obtained using the formula corrected for long correlation length (32). The original formula (29) overpredicts the diffuse, and therefore also total, intensity by 17.6% and 7.3%, respectively, in the specular direction. The corresponding errors after correction are 2.1% and 0.1%, respectively.

A similar improvement is observed for the P-P case with longitudinal incidence. An example for oblique incidence with $\theta_i = 15°$ for $\lambda_0 = \lambda_p \simeq 2\lambda_s$, $R = 50$mm is shown in Figure 7(b). Here, the ratio $\zeta = 3.30 < 4$ so the correction formula (32) is required. The uncorrected formula gives specular errors of 8.2% and 19.6% for the total and diffuse fields, respectively. These values are improved to, respectively, 2.1% and 3.5% after correction.

16

There are some interesting features of Figure 7(b) with respect to the shape and distribution of the scattering intensities. Oblique incidence highlights the shift in peak locations of the coherent and diffuse parts of the scattered field, which is not discernible for the case of normal incidence in Figure 7. The diffuse field is shifted progressively towards the backscattering angles, as the roughness increases. For these low $\sigma = \lambda/10$ values, the coherent field is still relatively strong, but as σ grows, the diffuse field starts to dominate such that the coherent peak vanishes completely, as will be illustrated in the next section where we consider cases without the need for correction.

4. Results

The cross-validation of the theoretical model, described in Sections 2 and 3, is performed using a combination of numerical, FE and experimental methods. The numerical simulations performed here use 4000 realisations but it is impractical to investigate 4000 surfaces using the FE method (each FE simulation takes 3 minutes per realisation for $R = 50$mm) so 400 realisations were analysed using FE methods [17, 8, 16] to validate KA theory, since such a number is more than sufficient to ensure the convergence for sample averaging. For those statistical parameter values where the error between KA and FE methods is below 1dB [17, 16], numerical simulations with thousands of realisations can then be run rapidly, and compared with the stationary phase theory.

4.1. Comparison of FE, KA and stationary phase results

In recent years, FE approaches have typically investigated between 50 and 100 rough surface realisations [11, 13, 17]. The latest advances made with the GPU-driven software package Pogo [27] have made it possible to run many more surfaces, at a much quicker rate. The investigation of the valid range of roughness for which KA theory applies to shear wave incidence [16] used 200 different realisations for each pair of statistical parameters σ and λ_0. The established bounds, summarised in Table 1, underpin the examples investigated in this article.

$\lambda_0(\lambda_{\mathrm{s}})$	$\sigma(\lambda_{\mathrm{s}})$							
	1/16	1/12	1/10	1/8	1/6	1/5	1/4	1/3
2	✓	✓	✓	✓	✓	✓	✓	✓
1	✓	✓	✓	✓	✓	✓	(✓)	×
1/2	✓	✓	✓	(✓)	×	×	×	×

Table 1: Range of validity of KA theory for incidence of plane shear waves for defects of length $L \geq 5\lambda_{\mathrm{s}}$ and $-15° \leq \theta_i \leq 15°$. Brackets indicate the threshold at which validity breaks down.

17

Here, larger samples of 400 realisations were used for FE validation, since an additional far field approximation is inherently assumed for the SPM when fixing the far field distance $R = 50$mm, measured from the centre of the rough surface, for all θ_s. For the MC KA and FE methods, this distance varies with each discretised facet, whereas those variations are neglected when applying SPM. Pure plane wave excitations are implemented (see [16] for details of these plus Gaussian windowed alternatives) using a five-cycle tone burst with a centre frequency of 5MHz. Defect length is $L = 8$mm, the dimensions of the FE model are 100×65 mm^2 and the absorbing layers are placed on all sides with a width of 5mm, following the recommended guidelines [28]. Linear triangular elements, whose dimension ensures that there are 30 elements per shear wavelength, are used and the time-step was chosen via a Courant number of 0.3 [28].

The plane wave is excited at a distance of 3mm from the centre of the defect, including the oblique incidence cases, where the defect is rotated, rather than the excitation line of nodes. The material parameters represent ferritic stainless steel, with $E = 210$ GPa, $\rho = 7900$ kg m^{-3} and $\nu = 0.31$. The theoretical wavelengths and wave speeds are $\lambda_s = 0.637$ mm, $c_s = 3185$ ms^{-1} and $\lambda_p = 1.21$ mm, $c_p = 6070$ ms^{-1}.

For each of three correlation lengths $\lambda_0 = 2\lambda_s, \lambda_s, \lambda_s/2$, various RMS values σ, as listed in Table 1, were analysed. Three examples are shown in Figure 8 for normal incidence, two within the valid range, and one outside. As can be seen from Table 1, the pairs $\lambda_0 = \lambda_s, \sigma = \lambda_s/6$ and $\lambda_0 = \lambda_s, \sigma = \lambda_s/4$ are expected to show good agreement for the FE and MC KA results. The plot of total intensity in dB versus θ_s in Figure 8(a) and (b) bear this out and also illustrate the good agreement with the stationary phase prediction given by the formulae (20), (29).

In contrast, the case of $\lambda_0 = \lambda_s/2, \sigma = \lambda_s/6$ illustrated in Figure 8(c) shows good agreement between the MC KA and stationary phase approaches, but a large error compared with the FE ensemble average. This result is predicted by Table 1 and is indicative of the general conclusion for shear waves that for $\lambda_0 = \lambda_s$, all three methods show good agreement. For $\lambda_0 = 2\lambda_s$, MC KA and FE methods show excellent agreement, but the stationary phase method overestimates intensity unless the correction outlined in Section 3 is applied. Finally, for $\lambda_0 = \lambda_s/2$, MC KA and SPM show good agreement, but once σ is sufficiently large, KA theory breaks down [16], and no longer agrees with the FE results.

These conclusions also hold for oblique incidence. An example for $\theta_i = -15°$ (as defined in Figure 1) is shown in Figure 9 for the same pair of roughness parameter values used in Figure 8(a). Thus, there should be good agreement between all three methods, and this is clearly shown in Figure 9(a) where the total intensity in dB is plotted versus θ_s. The FE result (dotted curve) veers away from the MC KA (solid) and SPM (dashed red) predictions as the scattering angles increase beyond the specular direction, but this is likely to be related to tip diffraction and multiple scattering effects that would be reduced by employing a Gaussian windowed plane wave. For the specular direction and peak of the diffuse field, the agreement is excellent. We also note that the MC KA result for $N = 4000$ (additional dashed black curve) shows negligible improvement over the dB scale, indicating that 400 FE surfaces are more than sufficient for validation.
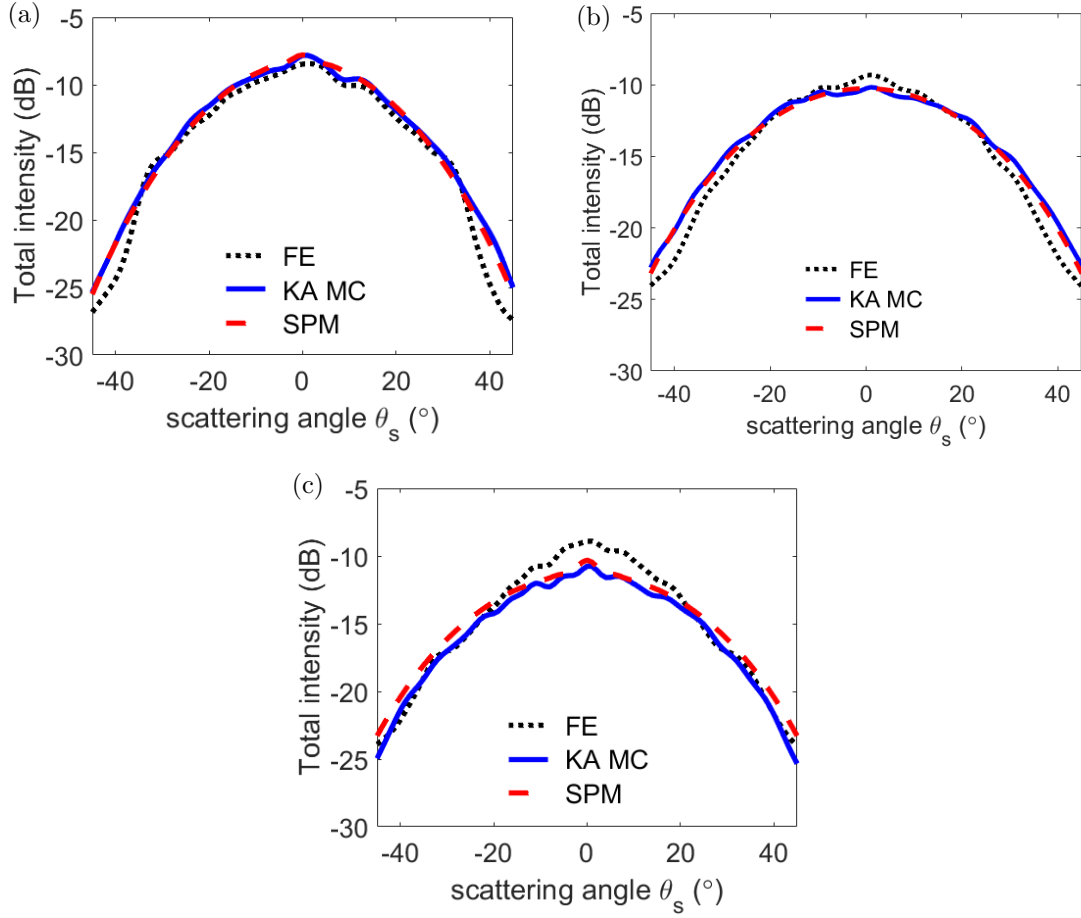
Figure 8: Total intensity (dB) of S-S mode for normal incidence plotted versus scattering angle θ_s with $R = 50$mm for MC KA (solid curve, $N = 400$), FE (dotted, $N = 400$) and SPM (dashed). (a) $\lambda_0 = \lambda_s, \sigma = \lambda_s/6$. (b) $\lambda_0 = \lambda_s, \sigma = \lambda_s/4$. (c) $\lambda_0 = \lambda_s/2, \sigma = \lambda_s/6$.

The same results are plotted using normalised intensities in Figure 9(b), to emphasise two things. Firstly, that the stationary phase ensemble average produces a rounder, more uniform shape than the MC KA results, although as N is increased the two plots converge, as shown by the additional dashed black curve for $N = 4000$ for MC KA. Secondly, as mentioned earlier at the end of Section 3, as σ is increased, the coherent intensity I^c decreases as the diffuse field dominates. The coherent results for both the FE and MC KA methods are shown in Figure 9(b).

4.2. Expected values and confidence bands

The major advantages of the stationary phase approach to obtain expected scattering intensity values are its speed of computation (< 1 second for all set-ups considered, using modern hardware) and its independence of specific roughness geometries (in practice, these are also unknown). To better validate the model and

19
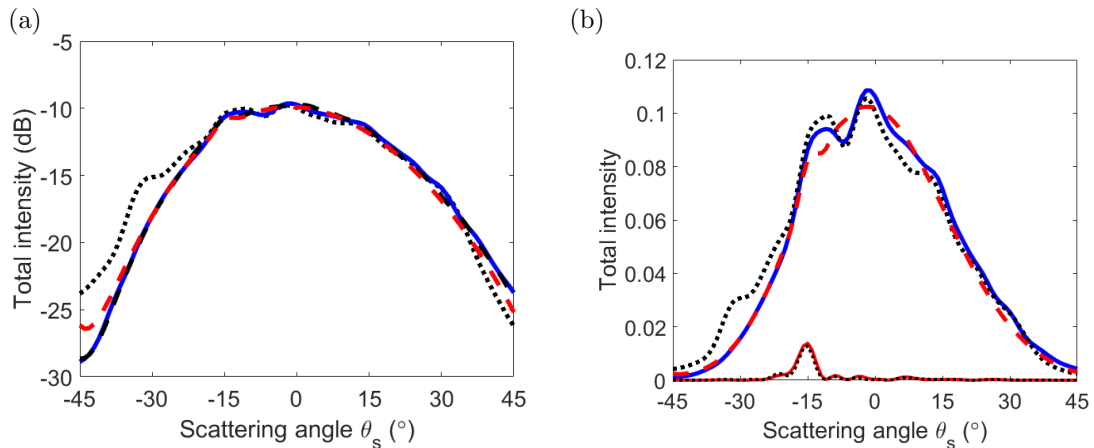
Figure 9: Total intensity of S-S mode for oblique incidence $\theta_i = -15°$ plotted versus scattering angle θ_s for MC KA (solid curve, $N = 400$), FE (dotted, $N = 400$) and SPM (dashed). $\lambda_0 = \lambda_s$, $\sigma = s/6$, $R = 50$mm. (a) Total intensity measured in dB, the additional dashed curve (black) represents the MC KA result for a set of 4000 surfaces. (b) Total intensity normalised using the specular peak for flat surface of the same dimension. Coherent field also shown.

its theoretical formulae (1), (20), (29), MC numerical simulations were carried out using several thousand realisations for roughness parameter values within the valid KA range, Table 1. Convergence tests showed that $N = 4000$ and $R = 50, 100$mm produced good results for both shear and longitudinal incidence, enabling direct comparison between both types of incident waves. Confidence bands of two standard deviations (95.4%) have also been calculated for each λ_0 for at least ten values of σ, including all of those listed in Table 1.

In Figure 10, we consider values of λ_0 that are approximately equivalent for shear wave and longitudinal incidence, recalling that $\kappa \simeq 1.9$ for ferritic steel, with $\lambda_0 = \lambda_s$ and $\lambda_p/2$, respectively. The far-field distance is $R = 50$mm for both wave-types and σ is determined as in Table 1, but plotted in mm in Figure 10 so that a direct comparison of S- and P-wave incidence can be made. We plot, respectively, total intensity and total reflected amplitude in the specular direction versus σ in Figures 10(a) and (b).

The solid curves show the S-S case, and the dashed curves denote the P-P modes. Confidence bands extending over two standard deviations (95.4%) are calculated for the 4000 surfaces and plotted either side of the mean intensities, plotted with $\times$ for S-S and $+$ for P-P, in Figure 10(a), and the mean amplitudes in Figure 10(b). The reduced validity range of KA for shear is evident since the shear curves terminate at RMS values less than half those seen for longitudinal incidence.

The confidence bands show some interesting trends. The lower band shows a significant drop when comparing results for specular intensity in Figure 10(a) with specular amplitude in Figure 10(b), whereas the upper band covers a similarly sized interval in both cases. This difference is to be expected from the calculation of intensity and amplitude, and their conversion to a dB scale. Intensity is proportional to
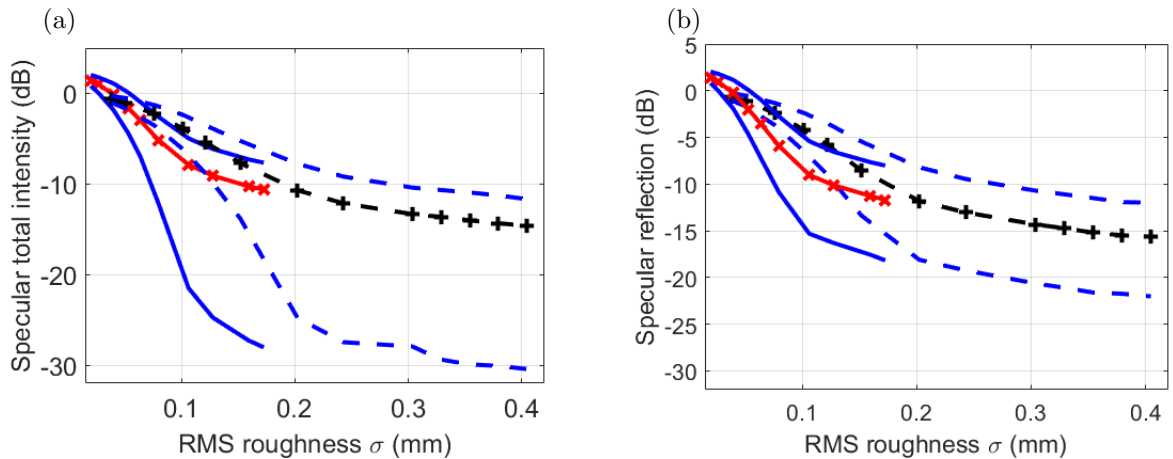
Figure 10: Total intensities and reflected amplitudes in specular direction for S-S (solid curves) and P-P (dashed curves) modes for normal incidence for cases of $\lambda_0 = \lambda_{\mathrm{s}}$, $\lambda_{\mathrm{p}}/2$. Confidence bands of 2 standard deviations (95.4%) are also shown. (a) Total specular intensity vs. σ. (b) Total specular amplitude vs. σ.

the square of amplitude; denoting the mean intensity as m_I and mean amplitude as m_A, the following conversions are used:

$$m_A(\mathrm{dB}) = 20 \log_{10}(m_A); \qquad m_I(\mathrm{dB}) = 10 \log_{10}(m_I). \tag{35}$$

The standard deviations (s_I, s_A) also have a quadratic relationship, so when converting the lower confidence bands (i.e. $m_A - s_A$ and $m_I - s_I \propto m_A^2 - s_A^2$) to dB, the amplitude has a dominant term $\propto 10 \log_{10}(m_A^2 + s_A^2)$ whereas the intensity has a dominant term $\propto 10 \log_{10}(m_A^2 - s_A^2)$, which translates to a significant difference on the dB scale. In contrast, for the upper band, both amplitude and intensity have a dominant term $\propto (m_A^2 + s_A^2)$, with the amplitude having an additional $2 m_A s_A$ term.

The shapes of the bands for shear and longitudinal incidence are similar, although for corresponding values of σ, amplitude and intensity drops for S-S modes are clearly much larger than for P-P modes. The value of the lower bound is critical, since it determines the safety margin for a practical ultrasonic inspection. It is also notable that the mean intensity and mean amplitude for P-P modes roughly match the upper confidence band for analogous shear cases for $\sigma \leq 0.15$mm, highlighting the contrast between the incident wave-types for rough surface scattering.

5. Experimental validations

Additional validation for the theoretical and Monte Carlo models was obtained through experimental methods. A rough surface was manufactured using a CNC (computer numerical control) milling machine on one face of an aluminium block ($230 \times 80 \times 30$ mm^3). The surface was corrugated so that the height remains invariant in the y-direction (see Figure 11) and the profile was generated using a Gaussian distribution of heights for the parameter values $\sigma = 0.3$mm and $\lambda_0 = 3$mm. For a centre frequency of 2MHz, these

roughness parameters roughly correspond to $\lambda_0 = 2\lambda_s$, $\sigma = \lambda_s/5$ so within the range of validity for KA
theory (see Table 1). An FE simulation of the experiment was performed using Pogo [27] to validate the
FE methods used in the preceding sections.

5.1. Experimental set-up parameters

Two ultrasonic phased arrays (Imasonic, Besançon, France) were used, with the transmitting array
attached (with couplant) to a rexolite wedge (Imasonic, Besançon, France) inclined at 34.75°, to produce
mode-converted incident shear waves. The receiving array was placed tightly next to the wedge, and the
two arrays systematically moved together across the top flat surface to insonify the maximum number of
rough surface sections that the sample size allowed. The experiment set-up is shown in Figure 11.
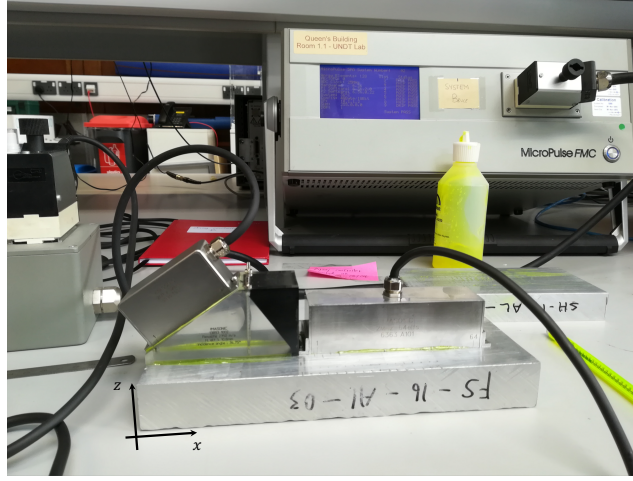
Figure 11: Experimental set-up with transmitting (on wedge) and receiving arrays placed on the top surface of an aluminium
block whose underside has been corrugated with a Gaussian randomly rough surface.

As can be seen from the photograph in Figure 11, the receiving array contains more elements (64)
than the transmitting (32) array. The receiving array was chosen to match as closely as possible the same
parameter values of the pitch and centre frequency as those of the transmitting array. The parameters for
both arrays and the rexolite wedge are summarised in Table 2. A preliminary experiment was performed
to determine the longitudinal wavespeed c_p^{Al} in the aluminium block prior to the manufacture of the rough
surface. The sample was placed in an immersion tank, on a computer-controlled platform, directly below
a partially submerged single crystal transducer (with a centre frequency of 10 MHz) connected to a signal
generator and oscilloscope. Measurements were performed at several locations across the surface of the
material, and at several depths within the water. The mean value obtained was $c_p^{Al} = 6330$ ms^{-1} which was
used via the standard bulk wave equations to obtain theoretical values for $c_s^{Al} = 3110$ ms^{-1} and the mode-
converted shear angle θ_i^{Al}, assuming the Young modulus and density of the aluminium to be, respectively,
$E = 70$GPa and $\rho = 2700$kg m^{-3}.

22

	Transmitting array	Receiving array
	Rexolite wedge, 2350 m/s, 34.75°	
Number of elements	32	64
Element width	22mm	22mm
Elementary pitch	1.5mm	1.57mm
Inter-element spacing	0.25mm	0.25mm
Centre frequency	2 MHz	2 MHz
Active length	47.75mm	100.23mm

Table 2: Parameter settings for phased arrays used in experimental set-up, replicated for the accompanying FE simulations.
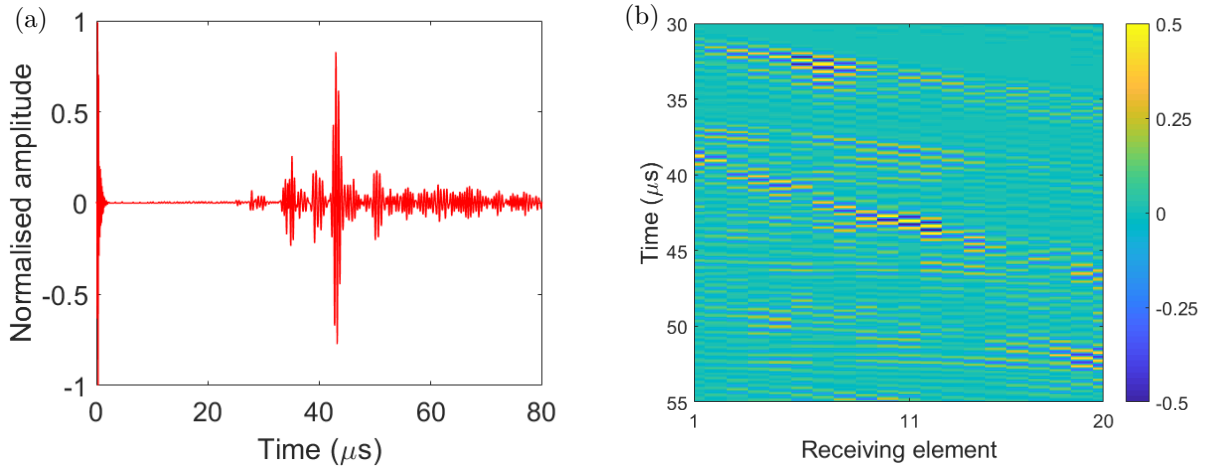

Figure 12: Images from BRAIN software (UoB) for rough surface corresponding to location 2. (a) Time domain signal for single transmitting element (20) to single receiving element (11), with the amplitude normalised to 1. (b) B-scan image of plane waves arriving at the first 20 receiving elements. The first arrival of S-S waves has large amplitude at element 11.

The theoretical expected incident angle for the shear waves mode-converted at the interface of the rexolite wedge and the aluminium sample is calculated using the Snell-Descartes law:

$$\frac{\sin \theta_i^{\mathrm{Al}}}{\sin \theta_i^{\mathrm{Rex}}} = \frac{c_{\mathrm{s}}^{\mathrm{Al}}}{c_{\mathrm{p}}^{\mathrm{Rex}}}; \qquad \theta_i^{\mathrm{Al}} = 48.95°. \tag{36}$$

This value, and those obtained for the wavespeeds, were used to generate a series of FE models to simulate the experiment. The FE models were constructed using Pogo [27], following similar methods to those used to validate the KA and stationary phase methods in Section 2 and [8, 4, 17, 16]. It follows that experimental validation of the FE method provides further validation of the theory and results of Sections 2 to 4.

The experiment set-up permitted measurements to be taken in 15 locations with the two arrays tightly arranged as shown in Figure 11, with the first 13 locations spaced 5mm apart, and the final two separated

23

by 10mm. The wedge-length is 88mm, so its end position ranged from 88mm to 168mm. As can be seen from the bottom row of Table 2, this allowed just over half of the receiving array's elements to be active for location 15. Five datasets were captured at each location using the MicroPulse FMC (Peak NDT, Derby, UK) ultrasonic array controller. The University of Bristol's (UoB) BRAIN software [29, 30] was used to obtain signals and images of the form shown in Figure 12, and to store full matrix capture (FMC) datasets [29] which were post-processed to obtain the results for comparison with the FE results. The shear wave is extracted using a time gate by estimating the arrival time of S-S waves from the wavespeed. For certain elements, some difficulty arises when surface waves and other reflections arrive with the S-S waves, as can be observed for elements 1-3 in Fig. 12(b).

5.2. Finite element simulation of the experiment

The fundamental building blocks of the FE simulations of the experimental set-up shown in Figure 11 follow those used for all previous validations [8, 4, 17, 16], i.e. ratio of element length to wavelength, time step, linear triangular elements, absorbing layer thickness etc. [28]. Additional specific details of the experimental set-up have been included in the Pogo models in this section, including the physical parameters of the rexolite wedge and its anti-reverberation material and the beam shape of the transmitting array (the source-line and number of cycles were adjusted). The flat aluminium surface was used to calibrate the FE models by determining the location of the backwall "origin" from which the scattering angles defined by the receiving array's elements were then measured.

The FE models were generated after careful measurement of all component parts of the experimental set-up and computation of the physical parameters, as summarised in Table 3. Figure 13 shows the FE

$c_\mathrm{p}^\mathrm{Rex}$	$c_\mathrm{s}^\mathrm{Rex}$	c_p^Al	c_s^Al	θ_i^Rex	θ_i^Al
2350 ms^{-1}	1150 ms^{-1}	6330 ms^{-1}	3110 ms^{-1}	34.75°	48.95°

Table 3: Physical parameter settings for FE simulations.

set-up and a snapshot of waves propagating within the sample for location 2 (i.e. the wedge has been placed 5mm from the origin in the x-direction). The snapshot is taken after the mode-converted shear wave has been scattered by the rough backwall, at a time of $t = 42.85\mu s$. Note that there is a strip of absorbing elements (width 10mm) on the right side of the wedge, which is used to mimic the wedge's anti-reverberation system. The rough surface was generated with the same dataset used to mill the aluminium block, and the lengths and heights obtained from the post-corrugated sample itself.

In the FE model, a source-line consisting of 32 nodes with the same elementary pitch and inter-element spacing as the real array, is excited on the surface of the wedge to generate a Gaussian tapered plane longitudinal wave [4] that travels through the rexolite at 34.75°. The chosen half beam width of $5\lambda_\mathrm{p}^\mathrm{Rex}$
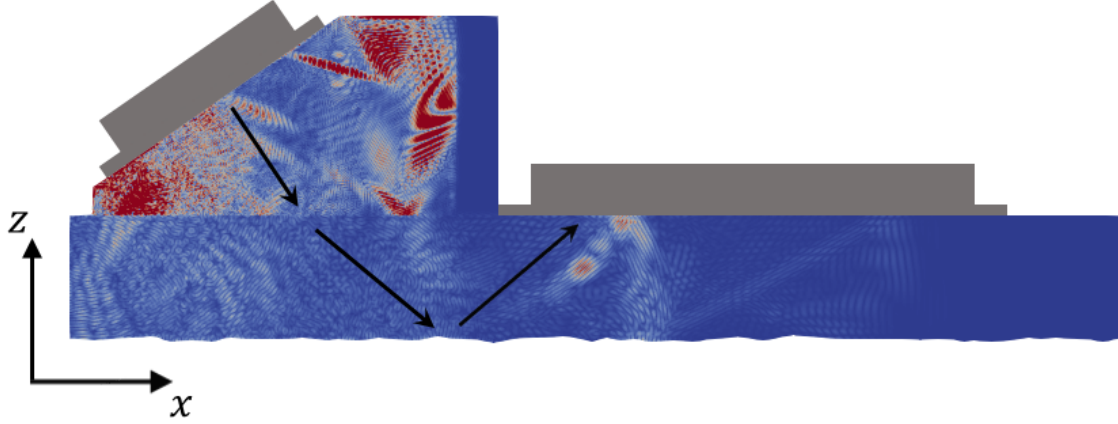
24

Figure 13: FE simulation snapshot at $t = 42.85\mu s$ for location 2. Total time for simulation is $T = 70\mu s$, absorbing layers of width 10mm are added to the right side of the rexolite wedge, all dimensions match those of the experimental set-up.

ensures that elements 9 to 24 are effectively fired with a Gaussian distribution of amplitudes; the use of such a Gaussian beam reduces edge effects [31], and a direct comparison can be made with the experiment by post-processing the FMC data to collate the corresponding receiving elements. At the interface of the rexolite and aluminium, mode conversion results in a shear wave that propagates to the rough backwall, where 15 sections of approximately 8mm $\simeq 12\lambda_\mathrm{s}^\mathrm{Al}$ are insonified in a sequential order.

The receiving array is simulated in a similar way, with 64 receiving nodes spaced to match the composition of the phased array. As in the case of the experiment, see Figure 12(a), the signals measured at the monitor nodes are complicated. An example is shown for location 2 in Figure 14(a) for receiving element 9. The large amplitude of the total displacement at around $42\mu s$ is consistent with both Figure 13, and with the area of large amplitude in the vicinity of receiving elements 9-11 in Figure 12(b) for the experiment.

5.3. Comparison of experimental and FE results

To accurately compare the experimental and FE results, the scattering angles θ_s corresponding to the receiving element locations have to be determined. For location 1, the flat uncorrugated aluminium block was used to determine the position of the virtual origin of scattering on the backwall (in mm) to be $(73.43, 0)$ by tuning with the FE simulation for the smooth backwall. The scattering angles were then simply computed relative to this origin using the known locations of the centres of the receiving elements. Since each subsequent location was determined by an increment of 5mm (or 10mm for locations 14 and 15), the virtual origin was shifted accordingly.

The first arrival of S-S scattered signals acts as the standard to validate the FE methods with the experimental measurements. The B-scan images (like that shown in Figure 12(b)) and FE visualisation snapshots (e.g. Figure 13) were used to identify a window of $37 - 48\mu s$ in which the first arrival of the S-S
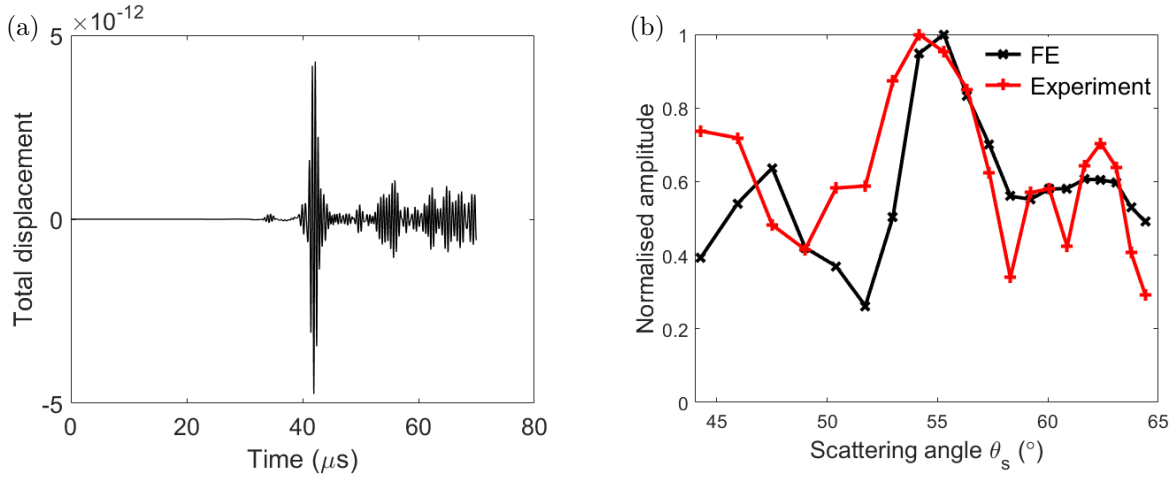
Figure 14: (a) FE time-domain signal (total displacement) for receiving element 9 ($\theta_s = 55.3°$) for rough surface location 2. (b) Comparison of FE method ('×') and experimental method ('+') for rough surface 2. Normalised amplitude vs. θ_s.

modes occurred, and that the first 20 receiving elements were sufficient to validate the S-S case. Receiving location signals beyond element $20/\theta_s = 65°$ (i.e. the remaining 44 elements) are not considered in this article, since they are subject to surface wave and secondary scattering signals, as can be seen in Figure 13.

The range of scattering angles considered is $44.3° \leq \theta_s \leq 64.4°$, with the specular direction being $48.95°$. The experimental datasets contain all possible element to element signals, since they were recorded using FMC. Post-processing is used to simulate a beam generated by the central elements of the transmitting array that is analogous to the tapered Gaussian plane wave simulated using the FE methods. Windowing and zero padding are then applied in both cases to isolate the S-S modes, and maxima of Hilbert peaks are found in both the time and frequency domains. Normalisation with respect to the maximum amplitude in the window $37 - 48\mu s$ is used to compare the experimental and FE results, since the amplitude of the FMC data obtained via the BRAIN software [29, 30] is scaled to unity.

An example for a specific rough surface (location 2) is shown in Figure 14(b). The amplitudes for the experiment (denoted by +) are normalised with respect to receiving element 8 or $\theta_s = 54.2°$ (since this was the largest Hilbert maximum amplitude in the window $37 - 48\mu s$) whereas the FE amplitudes (denoted by ×) have been normalised with respect to receiver 9's amplitude ($\theta_s = 55.3°$). Although there is this small shift of the peak, its location between $\theta_s = 53°$ and $57°$ is obtained from both the experimental and FE methods. There is also good qualitative agreement across the whole range of sampled scattering angles in Figure 14(b).

The results of Figure 14(b) are for one realisation only. To compare the total intensities, the first formula in (33) is employed for the 15 rough surface realisations, represented by the changes in location along the sample. The normalised total intensity (albeit normalised with respect to local maxima rather than a global
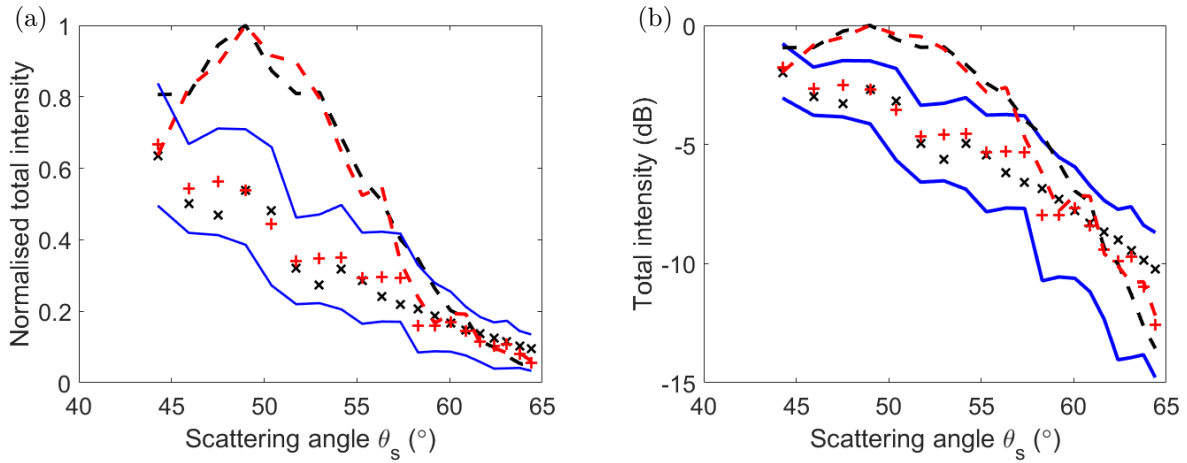
26

Figure 15: Comparison of experimental ('+') and FE ('×') results for 20 scattering angles, based on 15 realisations of rough surfaces characterised by $\lambda_0 = 3$mm and $\sigma = 0.3$mm. The incident angle is approximately $48.95°$. (a) Normalised total intensity versus scattering angle, (b) same as part (a) but on dB scale.

reference as in Figure 7) is plotted in Figure 15(a) versus the scattering angle for the experiment (+) and FE models (×). Figure 15(b) is plotted using the dB scale. The results for the flat surface are shown using the dashed curves, and confidence bands covering a width of two standard deviations are shown by the solid curves. The higher and lower (of FE or experimental) bands are used for, respectively, the upper and lower confidence bands. For smoother confidence curves, as in Figure 10, more than 15 realisations are required.

The results are very encouraging since the absolute error between the experimental and FE methods is < 1dB for 15 of the 20 scattering angles considered, and the exceptions are < 1.5dB except for the largest values of θ_s. The specular direction for this low roughness case (approximately $\lambda_0 = 2\lambda_{\mathrm{s}}, \sigma = \lambda_{\mathrm{s}}/5$) also sees fairly good agreement between the experimental and FE results, with only the second of the five values of θ_s that bracket the specular angle $\theta_s = 48.95°$, showing an error ≥ 1dB.

We note that the highest intensity/amplitude arises for a value of θ_s lower than the specular angle. This may be due to a number of reasons including attenuation in the couplant and/or aluminium leading to deviation of the specular angle from the expected value, the presence of additional surface waves contributing to the signals arriving at the first receiving elements and the roughness of the surface. The coherent intensity contributes around $80 - 85\%$ of the total intensity for $44.3° \leq \theta_s \leq 50.3°$ so it seems unlikely that only the roughness will lead to the shift of the specular peak. The fact that both the experiment and FE simulations detect the same shift provides further evidence of the fidelity of the FE validations performed using the Pogo software.

27

6. Conclusions

Many industrial ultrasonic NDE inspections use shear waves to detect and characterise rough defects, particularly in environments where higher sensitivity is crucial since the smaller wavelength is advantageous in comparison with longitudinal incidence. In environments subject to extreme changes in temperature and pressure, such as nuclear power station components, the damage that may occur is often far from uniform; rough cracks are formed and these are much more challenging to characterise, resulting in excessive conservatism for the qualification of ultrasound inspections.

A comprehensive study of shear wave incidence incorporating stochastic methods, numerical and experimental validations has been presented, whereby the expected reflection from a rough defect can be predicted reliably using a time-efficient statistical model. The reduced range of validity of the Kirchhoff approximation (KA) [16] highlights a hitherto uninvestigated dependence on correlation length for the application of the stationary phase method to both types of incidence. In Section 3, a correction term was introduced to the expected diffuse intensity for those cases when the ratio of correlation length to defect length exceeds a critical value, extending the range of applicability of the stochastic model.

The stationary phase adjustment to the KA integral was shown to be accurate upon validation against Monte Carlo simulations of several thousands of different surface profiles, for both longitudinal and shear wave incidence, using numerical and finite element (FE) methods. Experimental validations were also shown to give very encouraging results. We have also shown that for analogous roughness, the total scattering intensity is attenuated much more rapidly for shear waves than for longitudinal waves, and we have provided confidence bands covering two standard deviations for the expected values.

The advances in understanding the nature of scattering of shear waves by rough surfaces have great potential both for reducing the conservatism of presently qualified ultrasonic inspections in industry, and for proposing new methods for components and environments for which the established protocols are difficult to implement. The ability to rapidly estimate amplitudes, with associated confidence bands, will enable targeted inspection set-ups to be investigated, analysed and stringently validated in a more efficient manner.

References

[1] J. Ogilvy, Theory of wave scattering from random rough surfaces, CRC Press, 1991.

[2] C. A. Schultz, M. N. Toksöz, Enhanced backscattering of seismic waves from a highly irregular, random interface: P-sv case, Geophysical Journal International 117 (3) (1994) 783–810.

[3] Y.-C. Wen, C.-L. Hsieh, K.-H. Lin, H.-P. Chen, S.-C. Chin, C.-L. Hsiao, Y.-T. Lin, C.-S. Chang, Y.-C. Chang, L.-W. Tu, et al., Specular scattering probability of acoustic phonons in atomically flat interfaces, Physical review letters 103 (26) (2009) 264301.

[4] F. Shi, M. Lowe, R. Craster, Diffusely scattered and transmitted elastic waves by random rough solid-solid interfaces using an elastodynamic Kirchhoff approximation, Physical Review B 95 (21) (2017) 214305.

[5] R. S. Adler, D. K. Dedrick, T. J. Laing, E. H. Chiang, C. R. Meyer, P. H. Bland, J. M. Rubin, Quantitative assessment of cartilage surface roughness in osteoarthritis using high frequency ultrasound, Ultrasound in medicine & biology 18 (1) (1992) 51–58.

[6] B. N. Persson, O. Albohr, U. Tartaglino, A. Volokitin, E. Tosatti, On the nature of surface roughness with application to contact mechanics, sealing, rubber friction and adhesion, Journal of physics: Condensed matter 17 (1) (2004) R1.

[7] J. R. Pettit, A. E. Walker, M. J. Lowe, Improved detection of rough defects for ultrasonic nondestructive evaluation inspections based on finite element modeling of elastic wave scattering, IEEE Transactions on ultrasonics, ferroelectrics, and frequency control 62 (10) (2015) 1797–1808.

[8] F. Shi, M. Lowe, X. Xi, R. Craster, Diffuse scattered field of elastic waves from randomly rough surfaces using an analytical Kirchhoff theory, Journal of the Mechanics and Physics of Solids 92 (2016) 260–277.

[9] J. Ogilvy, Theoretical comparison of ultrasonic signal amplitudes from smooth and rough defects, NDT & E International 19 (1986) 371–385.

[10] J. Ogilvy, Computer simulation of acoustic wave scattering from rough surfaces, Journal of Physics D: Applied Physics 21 (2) (1988) 260–277.

[11] J. Zhang, B. W. Drinkwater, P. D. Wilcox, Longitudinal wave scattering from rough crack-like defects, IEEE transactions on ultrasonics, ferroelectrics, and frequency control 58 (10) (2011) 2171–2180.

[12] J. Zhang, B. W. Drinkwater, P. D. Wilcox, Effect of roughness on imaging and sizing rough crack-like defects using ultrasonic arrays, IEEE transactions on ultrasonics, ferroelectrics, and frequency control 59 (5) (2012) 939–948.

[13] R. A. Roberts, The effect of crack morphology on ultrasonic response, in: AIP Conference Proceedings, Vol. 1430, AIP, 2012, pp. 150–157.

[14] R. Long, J. Russell, P. Cawley, Ultrasonic phased array inspection using full matrix capture, Insight 54 (7) (2012) 380–385.

[15] R. Phillips, D. Duxbury, P. Huthwaite, M. Lowe, Simulating the ultrasonic scattering from complex surface-breaking defects with a three-dimensional hybrid model, NDT & E International 97 (2018) 32–41.

[16] S. Haslinger, M. Lowe, P. Huthwaite, R. Craster, F. Shi, Appraising Kirchhoff approximation theory for the scattering of elastic shear waves by randomly rough defects, Journal of Sound and Vibration (in press) (2019).

[17] F. Shi, W. Choi, M. Lowe, E. Skelton, R. Craster, The validity of Kirchhoff theory for scattering of elastic waves from rough surfaces, Proceedings of the Royal Society of London A: Mathematical, Physical and Engineering Sciences 471 (2178) (2015) 20140977.

[18] J. Achenbach, Wave Propagation in Elastic Solids, North-Holland Publishing Company/American Elsevier, 1973.

[19] J. Ogilvy, I. Culverwell, Elastic model for simulating ultrasonic inspection of smooth and rough defects, Ultrasonics 29 (6) (1991) 490–496.

[20] J. D. Achenbach, A. K. Gautesen, H. McMaken, Ray methods for waves in elastic solids: with applications to scattering by cracks, Pitman advanced publishing program, 1982.

[21] J. Achenbach, J. Achenbach, Reciprocity in elastodynamics, Cambridge University Press, 2003.

[22] P. Beckmann, A. Spizzichino, The scattering of electromagnetic waves from rough surfaces, Artech House Inc, Norwood, MA, 1987.

[23] M. Longuet-Higgins, Reflection and refraction at a random moving surface. i. pattern and paths of specular points, JOSA 50 (9) (1960) 838–844.

[24] M. V. Berry, Nature's optics and our understanding of light, Contemporary Physics 56 (1) (2015) 2–16.

[25] A. H. Harker, Elastic Waves in Solids, with applications to nondestructive testing of pipelines, Adam Hilger, 1988.

[26] A. S. Birks, R. E. Green, Nondestructive Testing Handbook: ultrasonic testing, American Society for Nondestructive Testing, 1991.

[27] P. Huthwaite, Accelerated finite element elastodynamic simulations using the GPU, Journal of Computational Physics 257 (2014) 687–707.

[28] P. Rajagopal, M. Drozdz, E. A. Skelton, M. J. Lowe, R. V. Craster, On the use of absorbing layers to simulate the propagation of elastic waves in unbounded isotropic media using commercially available finite element packages, NDT & E International 51 (2012) 30–40.

[29] C. Holmes, B. W. Drinkwater, P. D. Wilcox, Post-processing of the full matrix of ultrasonic transmit–receive array data for non-destructive evaluation, NDT & e International 38 (8) (2005) 701–711.

[30] J. Zhang, B. W. Drinkwater, P. D. Wilcox, A. J. Hunter, Defect detection using ultrasonic arrays: The multi-mode total focusing method, NDT & e International 43 (2) (2010) 123–133.

[31] C. A. Schultz, M. N. Toksöz, Enhanced backscattering of seismic waves from a highly irregular, random interface: P-SV case, Geophysical Journal International 117 (3) (1994) 783–810.